

Synthesis of CaThO₃ and SrThO₃ Nanoparticles for their Photocatalytic and Conductivity Properties

Sukhi Prakash¹, Vaishnavi P. S.¹, Ramesh S.¹, Devika P.D.^{1,*}

¹ School of Physical Sciences, Amrita Vishwa Vidyapeetham, Mysuru Campus, Mysuru – 570 026, Karnataka, India; sukhi.prakash09@gmail.com (S.P.); vaishnavi.ps17@gmail.com (V.P.S.); ramesh_s@my.amrita.edu (R.S.);

* Correspondence: devikad67944@gmail.com;

Received: 23.07.2024; Accepted: 15.07.2025; Published: 30.09.2025

Abstract: Herein, we describe the synthesis of CaThO₃ and SrThO₃ through the sol-gel method. Further, we have performed a detailed investigation into the structural, morphological, optical, electrical, and photocatalytic properties of the as-prepared MThO₃ (M = Ca and Sr) distorted Perovskite nanoparticles. Powder X-ray diffraction (PXRD) analysis confirmed the cubic crystal structure of the distorted perovskite, with further Rietveld refinement revealing the cubic crystal structure. The average crystallite sizes estimated by the Debye-Scherrer equation were 4.21 nm and 4.10 nm for CaThO₃ and SrThO₃, respectively. Scanning electron microscopy (SEM) studies reveal that the surface morphology of the as-prepared materials has an irregular shape, primarily due to the large amount of gas evolved during synthesis. Complex modulus dielectric analysis further elucidated the material's behavior, demonstrating changes in the real and imaginary parts of the dielectric modulus with frequency. The study also examined alternative current (AC) conductivity, with Jonscher's power law fitting revealing frequency-dependent conductivity behavior. Furthermore, optical absorbance studies revealed charge transfer bands in the UV-Vis-NIR range, with Kubelka-Munk analysis indicating estimated bandgaps of 4.2 and 4.1 eV for CaThO₃ and SrThO₃, respectively, consistent with their wide bandgap semiconductor nature. In addition, both CaThO₃ and SrThO₃ perovskites exhibited photocatalytic activity against methylene blue dye under tungsten halogen lamp irradiation, with significant reductions in dye concentration observed over 60 minutes.

Keywords: sol-gel method; Perovskite nanoparticles; Rietveld refinement; photocatalytic activity.

© 2025 by the authors. This article is an open-access article distributed under the terms and conditions of the Creative Commons Attribution (CC BY) license (<https://creativecommons.org/licenses/by/4.0/>), which permits unrestricted use, distribution, and reproduction in any medium, provided the original work is properly cited. The authors retain copyright of their work, and no permission is required from the authors or the publisher to reuse or distribute this article, as long as proper attribution is given to the original source.

1. Introduction

The sol-gel process is a low-temperature and cost-effective technique. Furthermore, such techniques control the chemical composition and concentration of dispersed dopants. This process enables better control over all the reactions involved in the synthesis of solids. Further, sol-gel method is useful for the fabrication of functional materials, such as photocatalysts, nonlinear optical materials, ferroelectrics, and superconductors [1]. Thorium is a promising element with significant applications, particularly in nuclear fuels, due to its ability to undergo nuclear fission and generate energy [2]. Additionally, thorium has been utilized for its photocatalytic properties [3]. Thorium, being a perovskite, has led some researchers to propose the use of perovskite oxides in various fields, including H₂ separation, O₂ separation, fuel cells, supercapacitors, solar cells, membrane reactors, water splitting, H₂ production, and the

reduction of carbon dioxide, methane, and environmental remediation. Perovskite oxide materials are considered promising photocatalysts for several potential photocatalytic applications due to their promising characteristics, such as compositional flexibility, excellent electronic, optical, magnetic, and overall resistance to photo-corrosion, as well as good thermal stability properties [4]. These properties are expected to enhance their desirable photocatalytic activity and high stability [5]. Among 2346 theoretically estimated single perovskite oxide structures, 265 have been successfully prepared. In this perspective, various single perovskite oxides, such as SrTiO₃, KTaO₃, NaTaO₃, KNbO₃, and NaNbO₃, have been reviewed, and it has been reported that their morphologies and surface properties strongly influence their photocatalytic activities [6]. Furthermore, the photocatalytic properties of these materials have demonstrated numerous applications in the field of solar-driven photocatalytic Hydrogen Evolution Reaction (HER) [7]. Recent studies on the progress of single perovskite oxides ABO₃-based photocatalysts, perovskite materials, and SrTiO₃-based photocatalysts for use in HER via water splitting were also reviewed [8]. The greatest advantage is that the chemical and physical properties of the materials obtained by the sol-gel method are related to the experimental conditions applied.

Thorium, when combined with strontium (strontium thorium oxide), where strontium oxide is a white crystalline solid, and thorium is a refractory material with a high melting point of approximately 3300°C (5972) [9]. Thorium is used as a form of nuclear fuel in some experimental and research reactors [10]. It helps in achieving better thermal properties and stability [11]. For the first time, the synthesis of SrThO₃ by a conventional solid-state route was reported in 1947 by Mary-Szabo [12]. Where SrThO₃ compounds fall under the category of “Perovskites” [13]. Despite being a nuclear fuel, it is also used in the production of specialty glasses and ceramics, as it acts as a flux, which helps lower the melting point of the material during manufacturing [14]. Additionally, it helps to maintain the thermal and mechanical strength of the final product [15]. On the other hand, thorium, when combined with calcium to form calcium thorium oxide, exhibits a Goldschmidt tolerance factor of 0.74, which falls under the orthorhombic or rhombohedral structure [16]. Both SrThO₃ and CaThO₃ exhibit good catalytic properties [17]. The presence of thorium oxide in combination with Ca and Sr can create active sites on the surface of the compound, allowing for a catalytic reaction [18]. Due to its nature, it has been utilized in various chemical reactions, including the oxidation of pollutants and the synthesis of chemicals. Additionally, this type of perovskite exhibits various electronic properties, including insulating, semiconducting, or even metallic behavior [19]. Hence, they are used in electronic devices and sensors [20]. As the world actively seeks suitable and reliable energy technologies to meet increasing energy demand and global climate goals, these thorium compounds are of greater importance [21].

In view of the above fact, we herein report the synthesis, structure, morphology, optical properties, electrical characteristics, and photocatalytic performance of SrThO₃ and CaThO₃ perovskite structures.

2. Materials and Methods

2.1. Experimental.

Calcium Thorium, produced by Avra Synthesis Pvt Ltd, is available in a 500 g pack size with a purity of approximately 95%. Thorium nitrate pentahydrate, from Isochem

Laboratories, is available in a 25 g pack size with a purity of approximately 99%. The PXRD measurements were conducted on an X-Pert Pro diffractometer at ambient temperature using a Cu-K α radiation source, and the results were collected over the 2 θ range of 10° to 80°. The absorption studies were performed on a UV-1800 spectrophotometer (Shimadzu, Japan).

2.2. Synthesis of MThO₃ (M = Ca and Sr).

The CaThO₃ and SrThO₃ nanoparticles were prepared using the sol-gel method [22]. Reagent-grade chemicals were used without further purification. Calcium hydroxide (1 mM) was mixed with thorium pentahydrate (0.5 mM) in deionized water (100 mL). To this, citric acid (9.6 g) was added, and the reaction mixture was stirred for 1 hour at room temperature, maintaining a pH of ~6 with the addition of an ammonia solution. The resulting pale-yellow solution was then stirred continuously at 60 °C until it formed a transparent, sticky gel. The gel was dried in a hot air oven at 200°C for 1 hour, which led to the formation of a lightweight, porous material due to the significant gas evolution. It was then sintered at 850°C for 4 hours to obtain a fine, homogeneous, dense powder.

2.3. Photocatalytic applications.

The synthesized CaThO₃ and SrThO₃ nanoparticles were tested for photocatalytic activity by degrading the methylene blue (MB) dye, performed at room temperature. Photocatalytic tests were performed under 150W tungsten halogen lamps as the light source. Distilled water was utilized to make the MB solution. Then, 50 mg of nanocatalyst was added to 80 mL of the MB solution, followed by stirring to ensure a homogeneous dispersion. The solution was then placed in the photoreactor at a distance from the 150W light source. At specific time points (0, 10, 30, and 50 minutes), portions of the solution were taken and centrifuged at 5000 rotations per minute for 5 minutes. The resulting solutions were further analyzed using a UV-visible spectrophotometer to investigate the photocatalytic process in more detail.

3. Results and Discussion

3.1. Powder X-ray diffraction studies.

The identification of the phases, lattice parameters, average crystallite sizes, and structural analysis of the nanoparticles were obtained using PXRD investigation [23]. The PXRD was indexed to the orthorhombic crystal perovskite system [24]. The experimentally observed and refined simulated XRD patterns are displayed in Figure 1. Most significant peaks from the experimentally observed pattern match the simulated pattern [25]. The size of crystallites in a compound was determined by analyzing the peak width of the XRD pattern. A broad and strong PXRD pattern indicates the formation of nano-sized crystallites. The Debye-Scherrer equation, as shown below, was used to calculate the crystallite size [26].

$$D = \frac{K\lambda\beta hkl}{\cos\theta} \quad (1)$$

Where D is used to indicate the crystallite size, K is employed as the symbol for the Scherrer constant, λ specifies the Cu K α radiation wavelength, β represents the FWHM value, and θ marks the Bragg angle. Based on the above methods, the average crystallite sizes of CaThO₃ and SrThO₃ nanoparticles were 73.5 nm and 118 nm, respectively (Tables 1 and 2).

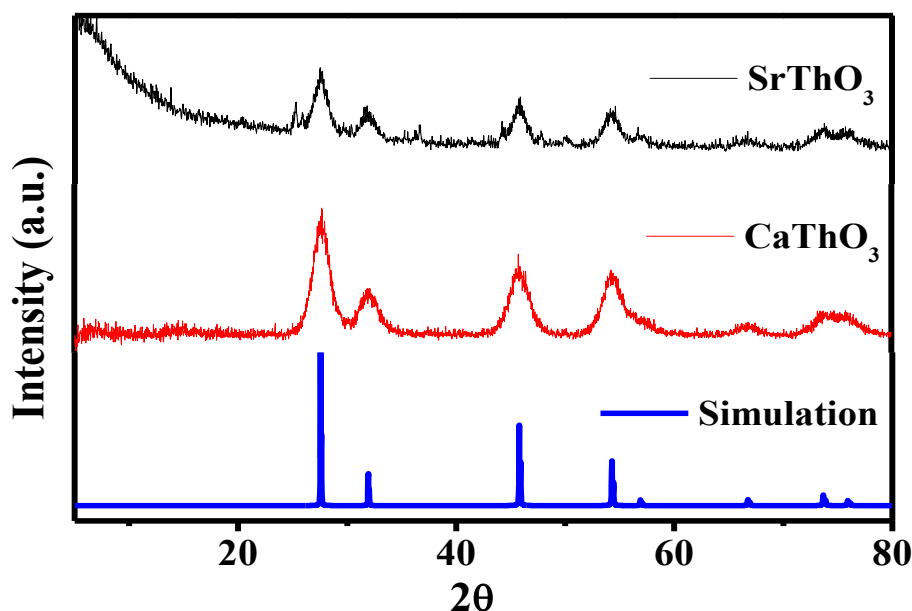


Figure 1. Powder X-ray diffraction of the MThO₃ (M=Ca, Sr) compared with the simulated pattern.

Table 1. Particle size of the CaThO₃ nanoparticles synthesized by sol-gel synthesis.

Pos. [° 2θ.]	FWHM Left [° 2θ.]	Size (nm)
27.7123	1.4170	60.42
31.9503	1.2595	68.65
45.6128	1.1021	81.82
54.2893	1.25951	74.17
73.6317	1.2595	82.45
Average Crystallite Sizes		73.502

Table 2. Particle size of the SrThO₃ nanoparticles synthesized by sol-gel synthesis.

Pos. [° 2θ]	FWHM [°2θ]	Size (nm)
20.4846	0.4723	178.85
25.1875	0.4723	180.34
27.5430	1.2595	67.95
31.7585	1.4170	60.99
36.4933	0.6298	138.98
45.7805	0.9446	85.53
Average Crystallite Sizes		118

3.2. Surface morphology studies.

The surface morphology and quantitative elemental composition of the sample were analyzed using scanning electron microscopy (SEM) images and energy-dispersive X-ray spectroscopy (EDS) analysis. Figure 2 presents SEM images and an EDX profile, showcasing the surface morphology at varying magnifications (20 μm, 3 μm, 2 μm, and 1 μm) and different randomly selected locations, as well as the elemental composition of SrThO₃ nanoparticles. We observe a heterogeneous picture, where particles of quite large size (1–20 μm) are mixed with smaller, undefined fragments. However, in a larger magnification picture (20 μm), it is apparent that each particle is indeed formed by an agglomeration of many smaller grains of typically 0.5–1 μm. Furthermore, we assume that these individual grains, like particles, are monocrystalline in nature, providing a sufficiently large diffraction domain that accounts for the significant crystallinity of the as-prepared material, as observed by neutron and X-ray synchrotron diffraction techniques.

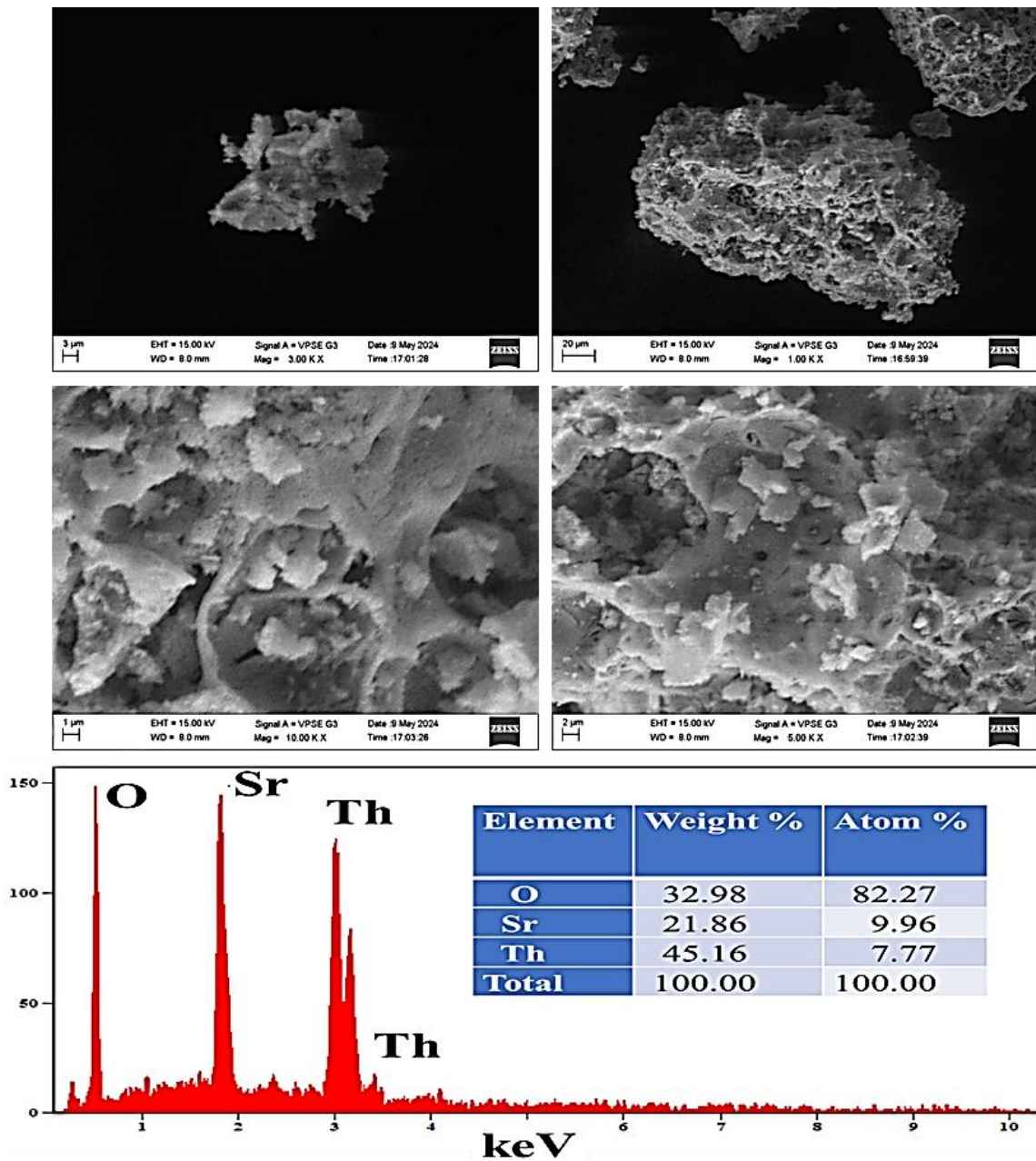


Figure 2. SEM images and EDX- profile, along with the quantitative analysis of SrThO₃ nanoparticles.

3.3. Impedance spectrum analysis of MThO₃ (Ca and Sr).

Impedance is a parameter that contains the resistive and reactive components. The impedance is plotted with log frequency on the X-axis and Z (real part) on the Y-axis. The study of impedance spectroscopy plays a significant role in analyzing the electrical characteristics of the homogeneous structure of the material. This method also helps us to distinguish between the insulating and conducting parts of the material. Figure 3 displays the frequency-dependent real component of the impedance Z' versus the frequency plot at room temperature. The real component of the impedance exhibits distinct behavior depending on the frequency range. At low frequencies, until 7.7×10^3 , the real part of the impedance decreases rapidly from 5×10^6 to 2.5×10^6 as the frequency increases, then the frequency gradually decreases. This can be explained by the increase in AC conductivity due to the higher mobility of charge carriers and the decrease in the concentration of trapped charges. At higher frequencies, the Z' curves approach a flat line, suggesting the potential release of space charge

polarization and subsequent reduction in barrier features within the material, as well as increased conductivity. This is inversely proportional to the frequency-dependent impedance spectral response, indicating that the study materials belong to the capacitive class. At the lower range, the sudden decrease is also associated with the relaxation processes being more accurate at lower frequencies for this material, as indicated by the behavior of the imaginary component of the impedance, Z'' . By understanding the imaginary impedance (Z'') spectra of the sample, we can acquire insights into the behavior of capacitor relaxation processes in materials [27].

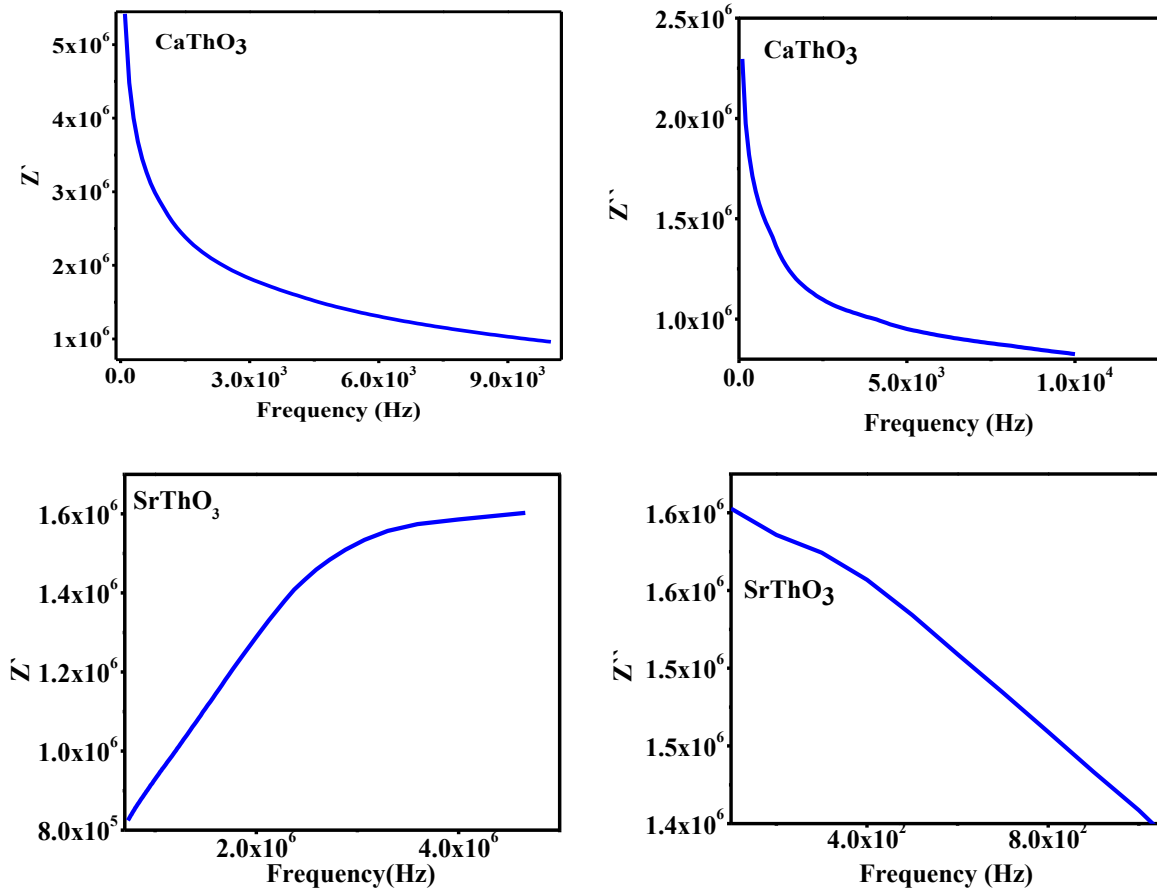


Figure 3. Frequency-dependent real and imaginary parts of the impedance spectra of the CaThO₃ (top row) and SrThO₃ (bottom row).

3.4. Optical absorbance studies.

Figure 4 depicts the UV–Vis–NIR diffuse reflectance spectra (DRS) of CaThO₃ and SrThO₃, which were attained in the range of 200–800 nm. In DRS, a strong broadband was seen in the range of 300–500 nm. This band is related to the charge transfer band (CTB), which is a band that transfers charge from the O²⁻ ligand to the Th⁴⁺/Sr²⁺ ions in the host lattice [28]. The optical bandgap energy is generally determined from measured diffuse reflectance spectra, which can be transformed into the corresponding absorption spectra by applying the Tauc plot (Equation 2) and the Kubelka–Munk equation (Equations 3 and 4). Although the K-M plot and the Tauc plot both evaluate the interaction between light and materials, the K-M plot is superior when it comes to materials that are opaque or scatter light and homogenous samples. When compared to Tauc plots, K-M plots are less susceptible to the effects of scattering and provide a more comprehensive picture since they consider both the effects of absorption and scattering. Because of this, K-M is a more suitable option for comprehending the entire light interaction

in samples of this kind. The optical bandgap of the materials was estimated using the Kubelka–Munk equation.

$$(\alpha h\nu)^{1/\gamma} = B (h\nu - E_g) \quad (2)$$

$$F(R) = K/S \quad F(R) = \frac{K}{S} = \frac{(1-R)^2}{2R} \quad (3)$$

Replacing the α with $F(R_\infty)$ in equation 2 it will become

$$(F(R) * h\nu)^{1/\gamma} = B (h\nu - E_g) \quad (4)$$

where h denotes the Planck constant, ν represents the frequency of the photon, E_g signifies the band gap energy, and B is a constant. The γ factor has a different value for the direct and indirect transition band gaps are 1/2 or 2, respectively, and is contingent upon the characteristics of the electron transition. The calculated bandgaps of CaThO_3 and SrThO_3 materials are found to be 4.2 eV and 4.19 eV, respectively, indicating that these materials belong to the wide bandgap semiconductor category.

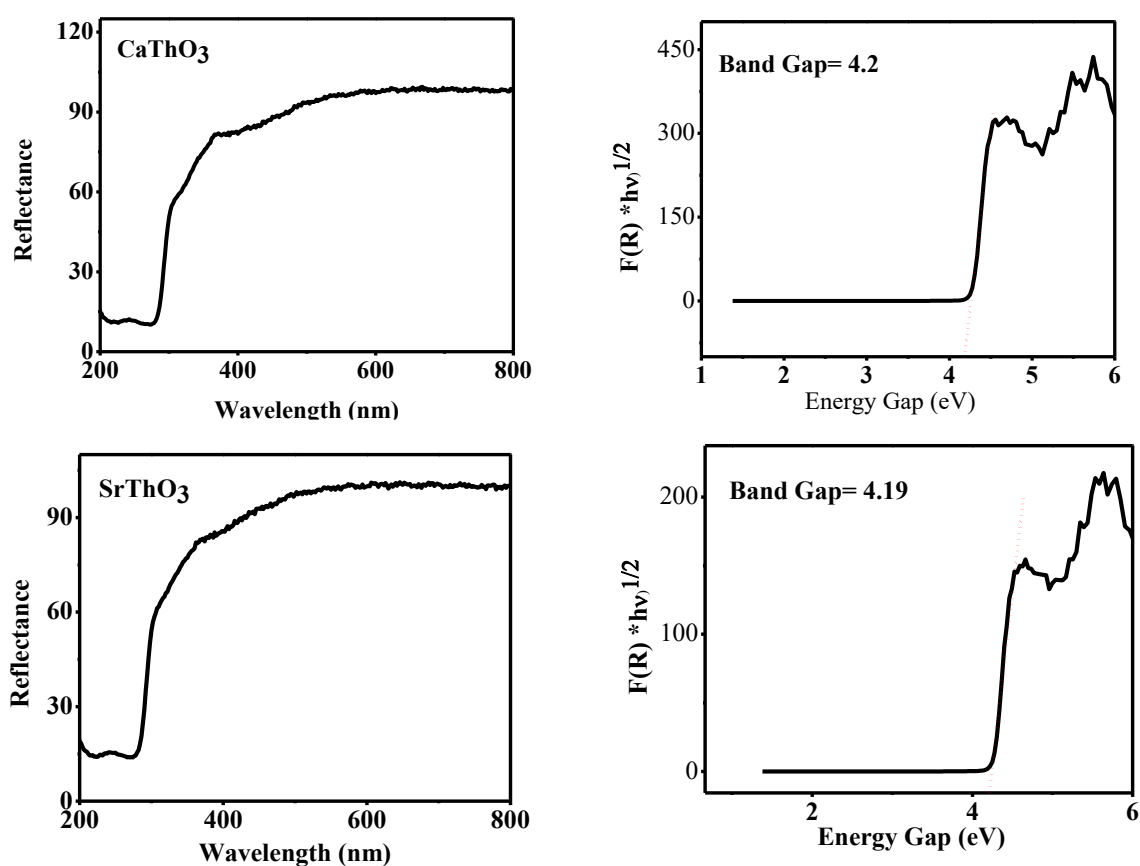


Figure 4. DRS spectrum at room temperature and (b) Kubelka-Munk bandgap of the CaThO_3 (top row), SrThO_3 (bottom row).

3.5. Photocatalysis studies.

The synthesized MThO_3 nanoparticles were tested for photocatalytic activity by degrading the methylene blue (MB) dye. Photocatalytic investigations of the as-prepared material were performed under a 150W tungsten halogen lamp as the light source. The MB solution was the target pollutant, with as-prepared nanoparticles acting as the catalyst. At different time intervals (0, 20, 40, and 60 minutes), portions of the solution were taken and centrifuged at 5000 revolutions per minute for 20 minutes. It is remarkable to note that 50% of the reduction was absorbed within 60 minutes due to the wide band gap of the materials. The

resulting solutions were further analyzed using a UV–visible spectrophotometer to investigate the photocatalytic process in more detail. The absorbance spectra of the photocatalytic dye degradation of the materials are shown in Figure 5.

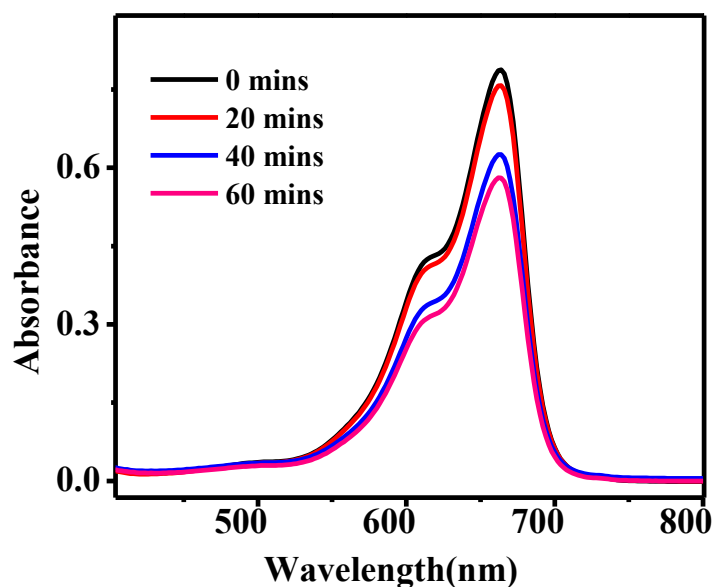


Figure 5. Photocatalysis (b) photocatalytic efficiency of the SrThO₃ nanoparticles.

4. Conclusion

To summarize, we have conducted a comprehensive investigation into the structural, morphological, optical, electrical, and photocatalytic properties of MThO₃ (M = Ca, Sr) distorted Perovskite nanoparticles. Powder X-ray diffraction analysis confirmed the cubic crystal structure of the distorted perovskite, with further Rietveld refinement revealing a cubic crystal structure with the F-423 space group for the studied distorted Perovskites. Surface morphology confirms that the irregular shape of the particles is due to a large amount of gas evolution during synthesis. The study also examined AC conductivity, with Jonscher's power law fitting revealing frequency-dependent conductivity behavior. The correlation between crystal structures and mechanical properties of molecular crystals, facilitated by advanced techniques, has provided insightful information on molecular conformation and crystal packing. Furthermore, the construction of an energy framework based on intermolecular interaction strength has provided a wealth of information on crystal structure, including the identification of active slip planes. Optical absorbance studies revealed charge transfer bands in the UV-Vis-NIR range, with Kubelka-Munk analysis indicating estimated bandgaps of 4.2 and 4.1 eV for CaThO₃ and SrThO₃, respectively, consistent with their wide bandgap semiconductor nature. Photocatalysis studies evaluated the materials' efficacy in degrading methylene blue dye under tungsten halogen lamp irradiation. Both CaThO₃ and SrThO₃ perovskites exhibited photocatalytic activity, with significant reductions in dye concentration observed over 60 minutes.

Author Contributions

conceptualization, D.P.D., S.P., R.S., and V.P.S.; methodology, S.P. and V.P.S.; software, D.P.D.; validation, V.P.S., D.P.D., and S.P.; formal analysis, S.P.; investigation, D.P.D.; resources, D.P.D.; data curation, S.P.; writing—original draft preparation, S.P. and V.P.S.; writing—review and editing, D.P.D.; visualization, S.P.; supervision, D.P.D.; project <https://nanobioletters.com/>

administration, D.P.D.; funding acquisition, D.P.D. All authors have read and agreed to the published version of the manuscript.

Institutional Review Board Statement

Not applicable.

Data Availability Statement

Data supporting the findings of this study are available upon reasonable request from the corresponding author.

Funding

This research received no external funding.

Acknowledgments

The authors extend their appreciation to the Director, Amrita Vishwa Vidyapeetham, Mysuru Campus, for providing instrumentation and infrastructure facilities.

Conflicts of Interest

The authors declare no conflict of interest.

References

1. Sakka, S. Chapter 11.1.2 - Sol–Gel Process and Applications. In Handbook of Advanced Ceramics (Second Edition), Somiya, S., Ed.; Academic Press: Oxford, **2013**; pp. 883-910, <https://doi.org/10.1016/B978-0-12-385469-8.00048-4>.
2. Vijayan, P.K.; Shivakumar, V.; Basu, S.; Sinha, R.K. Role of thorium in the Indian nuclear power programme. *Prog. Nucl. Energy* **2017**, *101*, 43-52, <https://doi.org/10.1016/j.pnucene.2017.02.005>.
3. Mohamed, N.A.; Ismail, A.F.; Safaei, J.; Johan, M.R.; Mat Teridi, M.A. A novel photoanode based on Thorium oxide (ThO₂) incorporated with graphitic Carbon nitride (g-C₃N₄) for Photoelectrochemical water splitting. *Appl. Surf. Sci.* **2021**, *569*, 151043, <https://doi.org/10.1016/j.apsusc.2021.151043>.
4. Nguyen, V.-H.; Do, H.H.; Van Nguyen, T.; Singh, P.; Raizada, P.; Sharma, A.; Sana, S.S.; Grace, A.N.; Shokouhimehr, M.; Ahn, S.H.; Xia, C.; Kim, S.Y.; Le, Q.V. Perovskite oxide-based photocatalysts for solar-driven hydrogen production: Progress and perspectives. *Sol. Energy* **2020**, *211*, 584-599, <https://doi.org/10.1016/j.solener.2020.09.078>.
5. Palharim, P.H.; D'Amara Caira, M.C.; Gusmão, C.; Ramos, B.; Gomes da Câmara, A.; A. Pacheco, J.G.; Rodrigues Jr, O.; Teixeira, A.C.S.C. Enhanced photocatalytic activity and stability of WO₃-AgCl/Ag composites: Surface modulation by structure-directing agents for effective sunlight treatment of pharmaceutical wastewater. *J. Photochem. Photobiol. A: Chem.* **2024**, *450*, 115433, <https://doi.org/10.1016/j.jphotochem.2023.115433>.
6. Taghizadeh, A.; Taghizadeh, M.; Sabzehmeidani, M.M.; Sadeghfar, F.; Ghaedi, M. Chapter 1 - Electronic structure: From basic principles to photocatalysis. In Interface Science and Technology, Ghaedi, M., Ed.; Elsevier: **2021**; Volume 32, pp. 1-53, <https://doi.org/10.1016/B978-0-12-818806-4.00010-3>.
7. Li, Y.; Liu, Y.; Zheng, T.; Liu, Z.; Levchenko, G.G.; Han, W.; Pashchenko, A.V.; Sasaki, S.-i.; Tamiaki, H.; Wang, X.-F. Hydrogen production by visible light photocatalysis with Chl@g-C₃N₄/Ti₃C₂T_x S-scheme heterojunction. *Appl. Surf. Sci.* **2023**, *640*, 158454, <https://doi.org/10.1016/j.apsusc.2023.158454>.
8. Subha, N.; Ravi Sankar, A.; Navaneethakrishnan, S.; Lavanya, J.; Aakash, M. Perovskite-based Z-scheme photocatalytic system for hydrogen production. *Catal. Commun.* **2024**, *187*, 106903, <https://doi.org/10.1016/j.catcom.2024.106903>.

9. Urakami, N.; Takashima, K.; Shimizu, M.; Hashimoto, Y. Thermal chemical vapor deposition of layered carbon nitride films under a hydrogen gas atmosphere. *CrystEngComm* **2023**, *25*, 877-883, <https://doi.org/10.1039/D2CE01515C>.
10. Chroneos, A.; Goulatis, I.; Daskalopulu, A.; Tsoukalas, L.H. Thorium fuel revisited. *Prog. Nucl. Energy* **2023**, *164*, 104839, <https://doi.org/10.1016/j.pnucene.2023.104839>.
11. Jyothi, R.K.; De Melo, L.G.T.C.; Santos, R.M.; Yoon, H.-S. An overview of thorium as a prospective natural resource for future energy. *Front. Energy Res.* **2023**, *11*, 1132611, <https://doi.org/10.3389/fenrg.2023.1132611>.
12. Hong, S.; Cheng, Y.; Hariyani, S.; Li, J.; Doughty, R.M.; Mantravadi, A.; Adeyemi, A.N.; Smith, E.A.; Brgoch, J.; Osterloh, F.E.; Zaikina, J.V. The Deep Eutectic Solvent Precipitation Synthesis of Metastable $Zn_4V_2O_9$. *Inorg. Chem.* **2022**, *61*, 154-169, <https://doi.org/10.1021/acs.inorgchem.1c02511>.
13. Deshmukh, V.V.; Ravikumar, C.R.; Kumar, M.R.A.; Ghotekar, S.; Kumar, A.N.; Jahagirdar, A.A.; Murthy, H.C.A. Structure, morphology and electrochemical properties of SrTiO₃ perovskite: Photocatalytic and supercapacitor applications. *Environ. Chem. Ecotoxicol.* **2021**, *3*, 241-248, <https://doi.org/10.1016/j.enceco.2021.07.001>.
14. García-Ten, J.; Dondi, M.; Vieira Lisboa, J.V.M.B.; Vicent Cabedo, M.; Pérez-Villarejo, L.; Rambaldi, E.; Zanelli, C. Critical raw materials in the global high-throughput ceramic industry. *Sustain. Mater. Technol.* **2024**, *39*, e00832, <https://doi.org/10.1016/j.susmat.2024.e00832>.
15. Caurant, D.; Majérus, O. Glasses and Glass-Ceramics for Nuclear Waste Immobilization. In *Encyclopedia of Materials: Technical Ceramics and Glasses*, Pomeroy, M., Ed.; Elsevier: Oxford, **2021**; pp. 762-789, <https://doi.org/10.1016/b978-0-12-818542-1.00090-4>.
16. Albrecht, E.K.; Karttunen, A.J. Investigation on the predictive power of tolerance factor τ for A-site double perovskite oxides. *Dalton Trans.* **2023**, *52*, 12461-12469, <https://doi.org/10.1039/D3DT01990J>.
17. Zou, J.-P.; Zhang, L.-Z.; Luo, S.-L.; Leng, L.-H.; Luo, X.-B.; Zhang, M.-J.; Luo, Y.; Guo, G.-C. Preparation and photocatalytic activities of two new Zn-doped SrTiO₃ and BaTiO₃ photocatalysts for hydrogen production from water without cocatalysts loading. *Int. J. Hydrogen Energy* **2012**, *37*, 17068-17077, <https://doi.org/10.1016/j.ijhydene.2012.08.133>.
18. Hours, C.; Claparede, L.; Reynier-Tronche, N.; Viallard, I.; Podor, R.; Dacheux, N. Dissolution of (U,Th)O₂ heterogeneous mixed oxides. *J. Nucl. Mater.* **2023**, *586*, 154658, <https://doi.org/10.1016/j.jnucmat.2023.154658>.
19. Assirey, E.A.R. Perovskite synthesis, properties and their related biochemical and industrial application. *Saudi Pharm. J.* **2019**, *27*, 817-829, <https://doi.org/10.1016/j.jsps.2019.05.003>.
20. Javaid, M.; Haleem, A.; Rab, S.; Pratap Singh, R.; Suman, R. Sensors for daily life: A review. *Sens. Int.* **2021**, *2*, 100121, <https://doi.org/10.1016/j.sintl.2021.100121>.
21. Dey, S.; Sreenivasulu, A.; Veerendra, G.T.N.; Rao, K.V.; Babu, P.S.S.A. Renewable energy present status and future potentials in India: An overview. *Innov. Green Dev.* **2022**, *1*, 100006, <https://doi.org/10.1016/j.igd.2022.100006>.
22. Bokov, D.; Turki Jalil, A.; Chupradit, S.; Suksatan, W.; Javed Ansari, M.; Shewael, I.H.; Valiev, G.H.; Kianfar, E. Nanomaterial by Sol-Gel Method: Synthesis and Application. *Adv. Mater. Sci. Eng.* **2021**, *2021*, 5102014, <https://doi.org/10.1155/2021/5102014>.
23. Mendenhall, M.H.; Henins, A.; Hudson, L.T.; Szabo, C.I.; Windover, D.; Cline, J.P. High-precision measurement of the x-ray Cu K α spectrum. *J. Phys. B: At. Mol. Opt. Phys.* **2017**, *50*, 115004, <https://doi.org/10.1088/1361-6455/aa6c4a>.
24. Sivasamy, R.; Venugopal, P.; Espinoza-González, R. Structure, electronic structure, optical and magnetic studies of double perovskite Gd₂MnFeO₆ nanoparticles: First principle and experimental studies. *Mater. Today Commun.* **2020**, *25*, 101603, <https://doi.org/10.1016/j.mtcomm.2020.101603>.
25. Holder, C.F.; Schaak, R.E. Tutorial on Powder X-ray Diffraction for Characterizing Nanoscale Materials. *ACS Nano* **2019**, *13*, 7359-7365, <https://doi.org/10.1021/acsnano.9b05157>.
26. Sivasamy, R.; Venugopal, P.; Mosquera, E. Synthesis of Gd₂O₃/CdO composite by sol-gel method: Structural, morphological, optical, electrochemical and magnetic studies. *Vacuum* **2020**, *175*, 109255, <https://doi.org/10.1016/j.vacuum.2020.109255>.
27. Floudas, G. 2.32 - Dielectric Spectroscopy. In *Polymer Science: A Comprehensive Reference*, Matyjaszewski, K., Möller, M., Eds.; Elsevier: Amsterdam, **2012**; pp. 825-845, <https://doi.org/10.1016/B978-0-444-53349-4.00057-1>.

28. Jyothi, G.; Gopchandran, K.G. Role of La³⁺ ion substitution sites on the photoluminescence properties of the SrTiO₃:Eu³⁺ phosphors. *J. Sci.: Adv. Mater. Devices* **2020**, *5*, 233-241, <https://doi.org/10.1016/j.jsamd.2020.04.006>.

Publisher's Note & Disclaimer

The statements, opinions, and data presented in this publication are solely those of the individual author(s) and contributor(s) and do not necessarily reflect the views of the publisher and/or the editor(s). The publisher and/or the editor(s) disclaim any responsibility for the accuracy, completeness, or reliability of the content. Neither the publisher nor the editor(s) assume any legal liability for any errors, omissions, or consequences arising from the use of the information presented in this publication. Furthermore, the publisher and/or the editor(s) disclaim any liability for any injury, damage, or loss to persons or property that may result from the use of any ideas, methods, instructions, or products mentioned in the content. Readers are encouraged to independently verify any information before relying on it, and the publisher assumes no responsibility for any consequences arising from the use of materials contained in this publication.